Introducing and Performance Assessment of a Novel Hybrid System Composed of MSW Plasma Gasification, and Combined Power Cycle (SOFC, ORC, and Carbon Dioxide Power)

Mehrpooya, Mehdi*+•

Department of Renewable Energies and Environment, Faculty of New Sciences and Technologies, University of Tehran, Tehran, I.R. IRAN

Ghorbani, Bahram

Faculty of Modern Technologies Engineering, Amol University of Special Modern Technologies, Amol, I.R. IRAN

Ardehali, Armin•

Department of Renewable Energies and Environment, Faculty of New Sciences and Technologies, University of Tehran, Tehran, I.R. IRAN

ABSTRACT: *Worldwide economic growth and rising urban population, along with rapidly growing urbanization and industrialization, have led to the unrelenting production of Municipal Solid Wastes (MSW). The concerns of rapid increase of energy demand consumption also concentrate the scientific attention on how to reuse the solid residues for generating bioenergy. The purpose of this article is to develop and introduce a novel MSW-driven plasma gasification system coupled with a carbon dioxide power cycle, organic Rankine cycle, and Solid Oxide Fuel Cell (SOFC), aimed at simultaneous waste management and power generation through an efficient and eco-friendly manner. The output of the MSW gasification process was used as a fuel of the SOFC system, and the sensible output heat of the SOFC is conducted to drive a combined power cycle; organic Rankine cycle and trans-critical carbon dioxide cycles. Aspen HYSYS/PLUS and MATLAB programming were used to model the developed structure. The SOFC and MSW plasma gasification process was validated and proved an appropriate approval. The output power generated by the integrated structure was calculated at 404.6 kW with 61.22%, 55.59%, and 21.53% for SOFC overall efficiency, gasification process energy efficiency, and overall thermal efficiency, correspondingly. The plasma energy ratio, Equivalence ratio, and steam-air mass ratio were defined to characterize the MSW plasma gasification process, and sensitivity analysis was applied to investigate the behavior of the system on different pressures, temperatures, air injection, and MSW mass flow rate. The sensitivity study revealed that*

*To whom correspondence should be addressed.

+ *E-mail: mehrpoya@ut.ac.ir*

• *Other Address: Hydrogen and Fuel Cell Laboratory, Faculty of New Sciences and Technologies, University of Tehran, Tehran, I.R. IRAN*

1021-9986/2023/8/2714-2734 21/$/7.01

the overall thermal and gasification process efficiencies increase up to 28.6% and 61%, respectively, when the MSW flow rate decreases from 400 to 250 kg/h.

KEYWORDS: *Municipal solid wastes; Plasma gasification; Solid oxide fuel cell; Carbon dioxide power cycle; Organic Rankine cycle; Sensitivity analysis.*

INTRODUCTION

Nowadays, economic growth and rising urban population, along with rapidly-growing urbanization and industrialization, have led to the unrelenting production of Municipal Solid Wastes (MSW) [1, 2], being accountable for major environmental problems particularly greenhouse gas emissions (about 16% of overall greenhouse gas emission) [3, 4]. Existing global MSW generation has reached roughly 1500 million tons/year [5], and is projected to rise to 2500 million tons/year by 2025 and 4200 million tons/year by 2050 [6]. The issues associated with MSW disposal, recycling, and treatment are substantial, but so are the prospects. Straight low-cost MSW disposal methods include landfilling, dumping, and incineration which significantly postponed environmental problems and health issues [7].

On the other hand, global challenges with respect to limited resources of fossil fuels and their environmental issues have long led to replacing the existing fossil fuels with affordable renewable sources [8]. According to the British multinational oil and gas company energy outlook report (2020) [9], the world's fastest-growing energy source belongs to renewable energies, providing half of the rise in worldwide energy supply, which is expected to contribute as the largest source of power by 2040. MSW, as a renewable source, has a considerable potential to be used for energy applications by exploiting various waste-to-energy (WtE) technologies which can seal the gap between energy and the environment by mitigating the environmental problems instigated by MSW [10]. To date, various WtE technologies for MSW treatment have been established, including combustion and incineration [10], anaerobic digestion [11, 12], refuse-drive fuel [13], pyrolysis [14], gasification and plasma-assisted gasification [15, 16], which in detail can be found somewhere else [17]. Plasma gasification, as one of the most efficient and clean WtE technology [17], converts the organic fraction of the MSW to high calorific value synthetic gas (mainly H_2 and CO). The plasma gasification employs a plasma torch as a high-temperature heat source (can even reach 10000 °C) to thermally decompose organic compounds and convert them to synthetic gas, while the inorganic part is vitrified to non-dangerous residues which can be organized and disposed safely [18, 19]. Even though the superiority of plasma gasification has been claimed by various authors [10, 17, 20, 21], but the main drawback is the severe electrical power requirement. A key solution is integrating the process of plasma gasification with other energy-efficient technologies like fuel cells [5, 22]. Fascinatingly, the produced synthetic gas through plasma gasification is rich in H_2 with a higher lower heating value [19], making it more suitable for integrating with fuel cells and various combined heat and power systems. Since hydrogen is an attractive fuel for the future, there are many studies on how to produce it and specifics of the production process based on its energy sources in three main categories [23].

Fuel cell is a promising candidate for clean and sustainable energy conversion. Among various types of fuel cells, Solid Oxide Fuel Cells (SOFC) have the advantages of high efficiency, fuel flexibility [24] (propane, glycerol, synthetic gas, natural gas), high-quality waste thermal energy, non-precious metal catalysts [24], and capability to integrate with other energy systems. In addition to these features, the higher operating temperatures of SOFCs (500-1000°C), make them more applicable to be integrated with various energy systems, e.g., heat, power and cooling cycles [25, 26], desalination cycles [27], biodiesel production [24], and various combined heat and power cycles aimed at enhancing the productivity and overall efficiency of the cycle.

Traditional stand-alone energy conversion technologies may hinder the reliable energy supply of future societies with huge and diverse energy demands, suffering from low efficiency, productivity, and

affordability [28]. To overcome this challenge, integrated energy systems have gained tremendous attention, and various studies have been focused on introducing and evaluating different integrated energy systems with the aim of improving energy utilization and promoting the exploitation of renewable energies [8]. In this regard and according to the background of this paper, *Yang et al.* [29] performed a techno-economic analysis of a WtE plant based on integrated intermediate pyrolysis and Combined Heat And Power (CHP) system. The proposed structure was capable of processing 5 tons of waste per hour and producing 4.4 MW electrical power and 5.3 MW thermal energy with an overall electrical efficiency of 27.2% and overall CHP efficiency of 59.7%. A new concept of integrating pyrolysis, anaerobic digestion, and CHP plants was presented by for the effective valorization of several fractions of MSW. The energy efficiency of the integrated structure was found to be 80%, while the efficiency of the standalone pyrolysis process was 60% [30]. Moreover, *Galeno et al*. [31] proposed the integration of a plasma torch gasification unit (fuel by refuse-derived fuel) and a solid oxide fuel cell system, producing 87 kW electricity with an electric efficiency of about 33%. Plasma gasifier reactor was studied by *Sakhraji et al*. [32] from a computational fluid dynamic viewpoint at approximately 1000 °K. Temperature distribution in the assumed gasifier fed by MSW is illustrated along with syngas. *Chen et al.* [33] proposed plasma-assisted gasification to deal with medical wastes. The syngas produced from gasification power gas turbine and combined cycle in an incineration plant. 3-E analysis has been done to demonstrate 4.24 MW net power with an energy efficiency of 37.83% to show that this system is auspicious and attainable. *Le et al.* [34] systematically reviewed arrangements of thermochemical conversions of WtE in a combination of renewable energies.

A thorough search of the literature showed that most of the research in the field of plasma-assisted WtE technologies focused on developing new mathematical models [35, 36], utilizing various feedstocks and gasifying agents [37, 38], developing new routes, mechanisms, and kinetics, thermodynamic, environmental and economic analyses [39]. At the same time, there is a lack in research to integrate plasma-assisted WtE with other compatible energy-efficient technologies to support the approval for commercial applications. To this aim, a novel the MSW-driven plasma gasification system coupled with a carbon dioxide power cycle, Organic Rankine Cycle (ORC), and solid oxide fuel cell was introduced and assessed. To the best of the authors' knowledge, this is the first attempt to integrate the MSW plasma gasification system with hybrid carbon dioxide/SOFC/ORC power cycles aimed at simultaneous waste management and power generation through an efficient and environmental-friendly means.

EXPERIMENTAL SECTION

In this study, a novel MSW plasma gasification system integrated with SOFC, ORC, and CO_2 power cycle for simultaneous waste management and power generation was introduced and assessed. The simulation process was developed by Aspen HYSYS/PLUS and MATLAB programming, and various sensitivity analyses were carried out to study the interplay role of operational parameters. The schematic flow diagram of the integrated structure is depicted in Fig. 1. In brief, the MSW at a rate of 300 kg/h along with air 60 kg/h and steam 100 kg/h, 1000 °C is directly fed to plasma gasification process and comes to contact with high-temperature plasma air (120 kg/h, 240 kW), where the organic fraction is transformed into valuable Synthetic Gas (SG) (555.4 kg/h), and the remaining inorganic fraction is converted to harmless vitrified slag that can be then valorized as a secondary product. The produced SG is then utilized as a fuel for the solid oxide fuel cell, producing 162.3 kW electricity and 598 kW heat. The produced heat within the SOFC system is further processed and used for electricity production through organic Rankine cycle and Carbon dioxide cycle at a rate of 24.35 and 217.8 kW, respectively. Overall, the proposed integrated structure is able to process and manage 300 kg/h MSW and produce 404.6 kW net electrical power.

Fig. 2 illustrates a detailed process flow diagram of the simulated integrated system. The system is composed of MSW plasma gasification system, solid oxide fuel cell process, organic Rankine cycle, and carbon dioxide power unit. The description and specification of each sub-processes within the integrated structure are presented in detail in the next subsections. Here is some assumptions are considered [40]:

1- Simulation of the integrated system is investigated under steady-state.

2- The pressure drops in pipes and heat exchangers are negligible.

3- Dead state is defined in 25 °C and 1 bar.

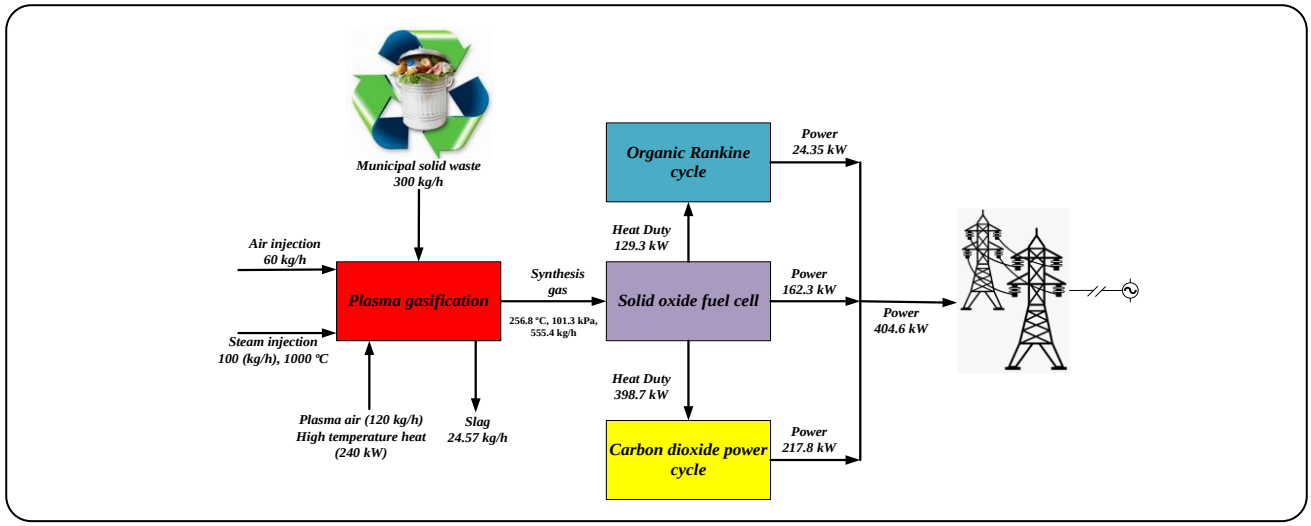

Fig. 1: The flowchart of integrated Plasma Gasification/SOFC/ORC/CO_2 power cycle hybrid system

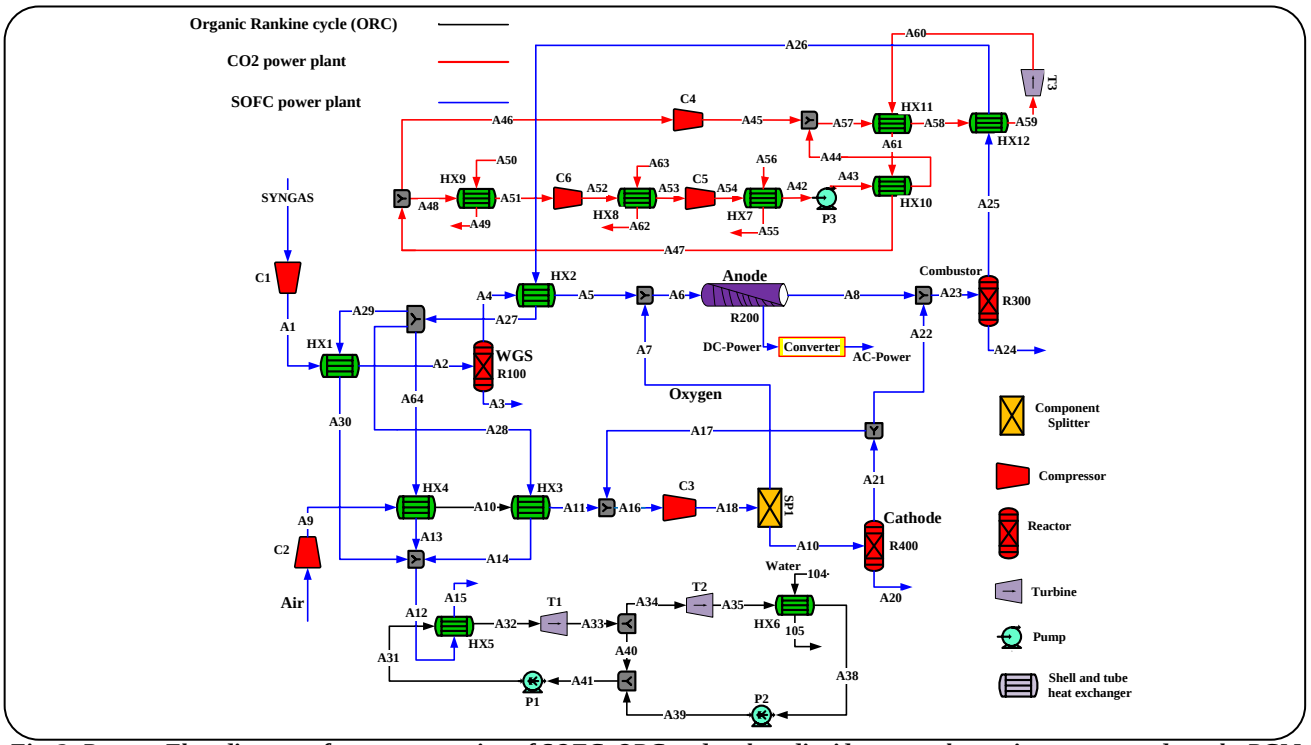

Fig. 2: Process Flow diagram of power generation of SOFC, ORC and carbon dioxide power plant using syngas produces by PGM

4- Heat losses from any subsystem are ignorable.

5- Adiabatic efficiency is considered at the constant percentage for turbines, compressors, and pumps in 80%, 75%, and 85%, respectively.

6- Pressure loss in reactors used in the gasification process is neglected.

7- RGibbs, RYield, RGibbs and RStoic reactors are considered for the gasification, decomposition, combustion and dryer sections, respectively.

MSW plasma gasification

As discussed before, plasma gasification was employed to process MSW and convert it to SG, as the most efficient and eco-friendly route for MSW treatment. The plasma gasification melting process was considered under the steady-state condition, which is divided into four main sections are described as follows. It is worth mentioning that the gas phase, which is composed of CO, CO_2, O_2, H_2, H_2O, N_2 and CH_4, flows upward. On the other hand,

Table 1: Detailed operational conditions of simulated plasma gasification

Stream	Temperature (ºC)	Pressure (kPa)	Mass flow (kg/h)	Molar Enthalpy (kJ/kgmole)	Molar Entropy (kJ/kgmole.K)
PLAS-AIR	25.0	101.3	120.0	-6.583	4.251
PLAS-AIR2	5765.5	101.3	120.0	207718.4	106.5
PLAS-AIR3	2000	101.3	120.0	66704.6	70.05
PLAS-AIR4	1745.7	101.3	120.0	57440.6	65.72
AIR-INJE	25.0	101.3	60.00	-6.583	4.251
AIR-MIX	1210.4	101.3	180.0	38291.5	54.71
STEAM	1000.0	101.3	100.0	-204084.5	9.901
CHAR1	626.3	101.3	98.81	-	-
COM-OUT	479.6	101.3	233.3	-155829.3	17.53
GAS	756.4	101.3	16.58	-50149.9	75.54
MSW-DRY	256.2	101.3	233.3	-	-
SYNGAS	256.8	101.3	555.4	-58885.4	179.7
PRO-GAS	626.3	101.3	488.7	-83503.3	59.13
SLAG	1800.0	101.3	24.57	-	-
DEC-OUT	256.2	101.3	233.3	-26310.1	19.28
COM-OUT	256.2	101.3	66.67	-233896.4	-24.69
MSW-WET	25.00	101.3	300.0	-	-

the solid phase processes downward, oppositely, while all the processes are occurring under atmospheric pressure, and there are no reflux inflows.

In the first section, raw MSW is heated through a dryer by hot syngas returned from below until reaching the temperature at 256.2 ˚C. The energy balance of heat in the exchanger is calculated as the following equation [41]:

$$\sum_i \dot{M}_i \int_{T_{syngas-out}}^{T_{syngas-in}} c_{p,i} dT = \dot{M}_{MSW-dry} \int_{T_{MSW-in}}^{T_{MSW-out}} c_{p,MSW-dry} dT + \dot{M}_{H_2O} \left(\frac{h_{ev}}{M_{H_2O}} + \int_{T_{MSW-in}}^{T_{syngas-out}} c_{p,H_2O} dT \right)$$

Dry MSW is prepared to undergo the pyrolysis section in two steps. First is decomposing materials to primary gas and tar and char renowned as primary pyrolysis. In the second reactor, tar production from the first step cracked to secondary tar and gas until it reaches 479.6 ˚C. it is crystal clear that the material characteristics and compositions of dry MSW form the reactions and production. Therefore, char residues from pyrolysis are conducted in the third section by separating from CHAR-SEP to meet the 626.3 ˚C in 98.81 kg/h mass flow rate. In the combustion unit, high-temperature steam at 1000 ˚C, and 1210.4 ˚C air with 100 kg/h and 180 kg/h flow rate, respectively, is injected into the Gibbs reactor for char gasification. Since then, the number of inorganic non-combustible materials remaining from the combustion section is conducted to the melting process by separator for the last stage. Surrounded air is heated by PLASMA-G to reach the temperature at 5765.5 ˚C to prepare for melting the ashes. To be more precise, strong electricity under high potential voltage is passed through arcs which ionize pressurized inert gas [42]. Hazardous wastes are melted at high temperatures, and vitrified slags lead outward. On the other hand, the PLAS-AIR4 is mixed with additional air for recycling in the combustion unit. The simulated flow diagram in Aspen PLUS is presented by Fig. 3.

Table 1 lists the operational conditions of simulated plasma gasification.

Table 2 describes the molar fractions of some major flows in the developed integrated structure from syngas produced by the MSW gasification.

The lower heating value of MSW can be calculated as follows [43]:

$$LHV_{MSW} = HHV_{MSW} - 9h_{fg}$$

Table 2: Specifications of molar fractions of major flows in developed integrated process from syngas of MSW gasifier

Stream	CH_4	C_2H_6	H_2	H_2O	CO_2	CO	N_2	O_2	R-113
SYNGAS	0.0484	0	0.2322	0.2650	0.0874	0.1849	0.1820	0	0
A4	0.0484	0	0.3193	0.1779	0.1745	0.0.977	0.1820	0	0
A6	0.0441	0	0.1930	0.0153	0.0662	0.1796	0.1657	0.3350	0
A7	0	0	0	0	0	0	0	1	0
A8	0	0	0.0909	0.4508	0.2405	0.0519	0.1659	0	0
A12	0	0	0	0.1463	0.0790	0	0.6808	0.0.938	0
Air	0	0	0	0	0	0	0.7900	0.2100	0
A16	0	0	0	0	0	0	0.7968	0.2032	0
A21	0	0	0	0	0	0	0.8011	0.1989	0
A22	0.	0	0.0241	0.1195	0.0637	0.0137	0.6680	0.1110	0
A32	0	0	0	0	0	0	0	0	1
A36	0	0	0	1	0	0	0	0	0
A43	0	0	0	0	1	0	0	0	0
A56	0	0	0	1	0	0	0	0	0
A62	0	0	0	1	0	0	0	0	0

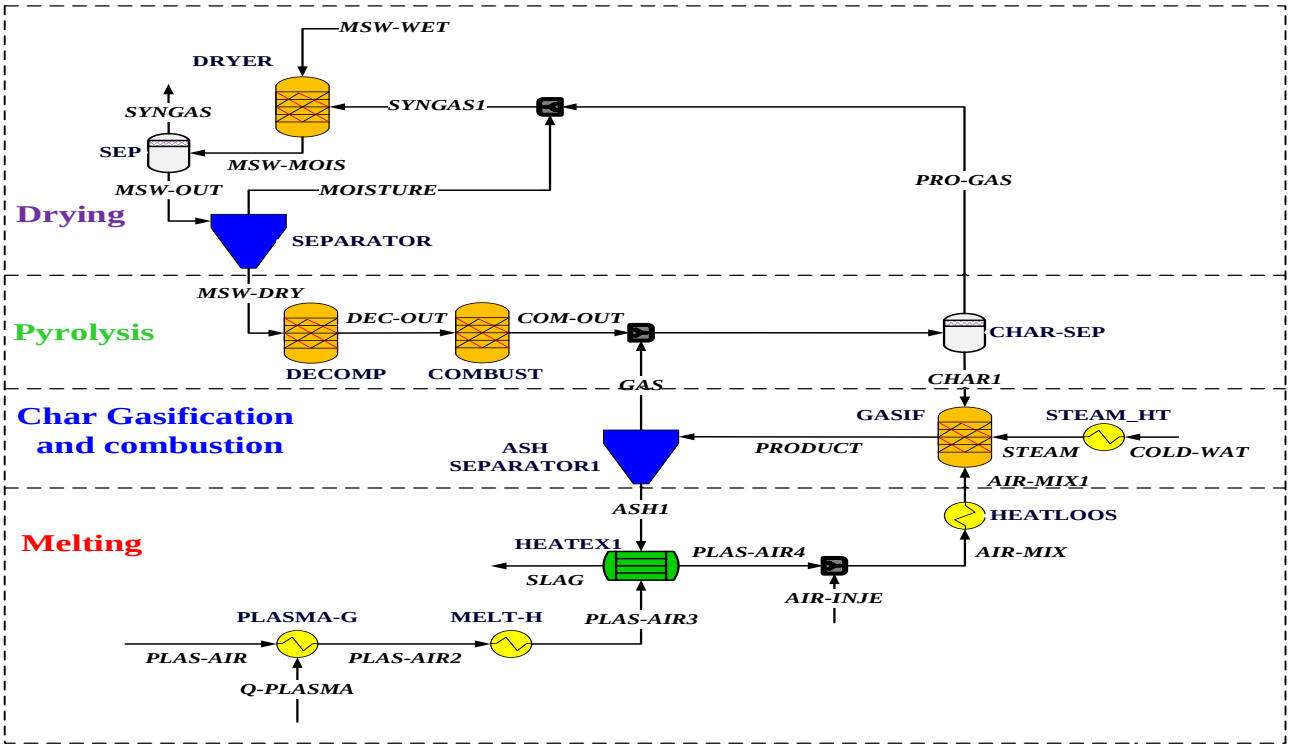

Fig. 3: Plasma gasification flow sheet

Whereas, the Higher Heating Value (HHV) defined by [43]:

$$HHV_{MSW} = 0.3491C + 1.1783H + 0.10051S - 0.10340O - 0.015N - 0.0211Ash$$

For quantifying system performance, three dimensionless parameters are introduced as follows:

Equivalence Ratio (ER) represents the first dimensionless parameter in the intensity of combustion by the amount of air is injected for oxidization in the char gasification process [21]:

$$ER = \frac{(\dot{m}_{air}/\dot{m}_{MSW})}{(\dot{m}_{air}/\dot{m}_{MSW})_{stoic}} \quad (2)$$

Since the amount of sensible heat and high temperature is supplied by PGM technology where it is fed with largely extent of voltage and electricity. The Plasma Energy Ratio (PER) is characterized by following system performance more accurately [40]:

$$PER = \frac{P_{plasma}}{LHV_{MSW}.\dot{m}_{MSW}} \quad (3)$$

The Steam-Air Mass Ratio (SAMR) introduced the share of steam mixed with air both support char gasifier while steam commonly applied for enhancement of the gasification process. It is defined as mentioned [40]:

$$SAMR = \frac{\dot{m}_{steam}}{\dot{m}_{air}} \quad (4)$$

SOFC system

A high variety of fuels as a feed of fuel cell, low emissivity, and high operating temperature becomes the SOFC as an environmental-friendly candidate to be integrated with cycle [44]. Syngas produced by plasma gasification containing 0.2650 H_2O, 0.2322 H_2, 0.1849 CO, 0.1820 N_2, and 0.0484 CH_4 is compressed and heated by C1 and HX1, respectively, until reach 642.5 ˚C and 129 kPa, which is prepared for reformer (R100). Overall, the reaction in the reformer is formed by endothermic and exothermic reactions for reaching the adequate hydrogen to the anode side.

Steam methane reforming:

$$CH_4 + H_2O \Rightarrow CO + 3H_2 \quad (5)$$

Water-gas shifting:

$$CO + H_2O \Rightarrow CO_2 + H_2 \quad (6)$$

And the final reaction is attained as follow:

$$CH_4 + 2H_2O \Rightarrow CO_2 + 4H_2 \quad (7)$$

Although several models are proposed for WGS and SMR reactions, the kinetics are formulated based on the type of catalyst and operating conditions. Using commercial catalyst Ni/a-Al_2O_3 in 120-600 kPa and 748-823 K pressure and temperature ranges, respectively, studied by *Hou et al*, [45] stand on Freundlich's adsorption model and (LH-HW) method. Steady-state, plug flow, scarce pressure drop (maximum 20 kPa), isothermal condition, and no interphase mass transfer constraint are considered as main assumptions [45]. Reaction kinetics are derived by the following equations [46]:

$$r_1 = \frac{K_1}{(P_{H_2})^{1.25}} \times \left(\frac{(P_{CH4}) \times (P_{H_2O})^{0.5} - \left(\frac{P_{CO} \times (P_{H_2})^3}{K_{P1} \times (P_{H_2O})^{0.5}} \right)}{(DEN)^2} \right) \quad (8)$$

$$K_1 = 5.922 \times 10^8 \times e^{\frac{-2.09\times10^5}{RT}}$$

$$K_{P1} = 1.198 \times 10^{17} \times e^{\frac{-2.683\times10^4}{T}}$$

$$r_2 = \frac{K_2}{(P_{H_2})^{0.25}} \times \left(\frac{(P_{CO}) \times (P_{H_2O})^{0.5} - \left(\frac{P_{CO_2} \times P_{H_2}}{K_{P2} \times (P_{H_2O})^{0.5}} \right)}{(DEN)^2} \right) \quad (9)$$

$$K_2 = 6.028 \times 10^{-4} \times e^{\frac{-1.5\times10^4}{RT}}$$

$$K_{P2} = 1.767 \times 10^{-2} \times e^{\frac{4.4\times10^3}{T}}$$

$$r_3 = \frac{K_3}{(P_{H_2})^{1.75}} \times \left(\frac{(P_{CH_4}) \times (P_{H_2O}) - \left(\frac{P_{CO_2} \times (P_{H_2})^4}{K_{P3} \times (P_{H_2O})} \right)}{(DEN)^2} \right) \quad (10)$$

$$K_3 = 1.093 \times 10^3 \times e^{\frac{-1.094\times10^5}{RT}}$$

$$K_{P3} = 2.117 \times 10^{15} \times e^{\frac{2.243\times10^4}{T}}$$

$$DEN = 1 + (5.127 \times 10^{-13} \times e^{\frac{131518}{T}})P_{CO} + (5.68 \times 10^{-10} \times e^{\frac{11234}{T}})P_{H_2}^{0.5} + (9.25 \times 10^{-10} \times e^{\frac{-1912}{T}})\frac{P_{H_2O}}{P_{H_2}} \quad (11)$$

Where P_i representing each partial pressure (kPa), k_i denoting reaction rate constant (kmol. kPa/kgcat) and K_i denoting absorption coefficient (1/kPa).

Heating the steam reforming (A4) in the HX2 exchanger raises its temperature to 768.5 ˚C before feeding to the anode side with the proper components of 0.3350 O_2, 0.1930 H_2, 0.1796 CO, 0.1657 N_2, 0.0662 CO_2, 0.0441 CH_4, 0.0153 H_2O molars based.

From the other, stream A18, with a flow rate of 6431.5 kg/h, which is heated and compressed by two heat exchangers (HX3, HX4) and two compressors (C2, C3), is prepared for reduction, followed by the cathode side as below [47]:

$$\frac{1}{2}O_2 + 2e^- \Rightarrow O^{2-} \quad (12)$$

In the anode side injected fuel (A6) with a mass rate of 755 kg/h is oxidized to produce water, electricity and carbon dioxide. Such as [47]:

$$H\_2 + O\^(2-) \Rightarrow H\_2\,O + 2e\^ -$$
$$CO + O\^(2-) \Rightarrow CO\_2 + 2e\^ - \quad (13)$$
$$CH\_4 + 4O\^(2-) \Rightarrow CO\_2 + 2H\_2\,O + 8e\^ -$$

SOFC voltage

To calculate the net voltage of the actual cell, three main losses should be reduced from the ideal voltage (V_N). This can be defined as follows [48]:

$$V_{cell} = V_N - (V_{act} + V_{conc} + V_{ohm}) \quad (14)$$

In which V_{act}, $V_{conc}$and V_{ohm}stand for activation, concentration and, ohmic losses, accordingly. Reversible voltage is attained from Nernst equation [49]:

$$V_N = 1.177 - 0.06855(t-1) - 0.0165(t\,ln\,t - t) + \frac{RT}{n_eF} ln(\frac{(P_{O_2}^0)^{0.5}(P_{H_2}{}^0)}{P_{H_2O}^0}) \quad (15)$$

$$t = \frac{T}{298.15} \quad (16)$$

Where T represents the cell temperature and P_i^0denotes the bulk pressure fraction of specific species.

Resistance of each of the components combined together effects the voltage drop to be weighty, which is formulated by Ohm law [49]:

$$V_{ohmic} = j \times \sum_i \frac{\delta_i}{\sigma_i} \quad (17)$$

$$J=J_0\left[\exp\left(\frac{\alpha n_e F}{RT}V_{act}\right) - \exp\left(\frac{-(1-\alpha)n_eF}{RT}V_{act}\right)\right] \quad (18)$$

On the other hand, the prime energy uses to activation the cells causes some losses, derived by these equations [50]:

$$V_{act} = \frac{2RT}{n_eF}\left(sinh^{-1}\left(\frac{j}{2j_{0,cat}}\right) + sinh^{-1}\left(\frac{j}{2j_{0,an}}\right)\right) \quad (19)$$

$$j_{0,cat} = \frac{RT\gamma_{cat}}{N_eF} \times exp(-\frac{E_{act,cat}}{RT}) \quad (20)$$

$$j_{0,an} = \frac{RT\gamma_{an}}{N_eF} \times exp(-\frac{E_{act,an}}{RT}) \quad (21)$$

By applying Fick's law under constant current assumed, concentration voltage loss is expressed as below [51]:

$$V_{conc} = \frac{RT}{n_eF} \times \left(\ln\left(\frac{P_{H_2}^0 \times P_{H_2O}^*}{P_{H_2}^* \times P_{H_2O}^0}\right) + \ln\left(\frac{P_{O_2}^0}{P_{O_2}^*}\right)^{0.5}\right) \quad (22)$$

$$P_{H_2}^* = P_{H_2}^0 - \frac{RTJ\delta_{an}}{n_eFD_{H_2}^{eff}} \quad (23)$$

$$P_{H_2O}^* = P_{H_2O}^0 - \frac{RTJ\delta_{an}}{n_eFD_{H_2O}^{eff}} \quad (24)$$

$$P_{O_2}^* = P_{O_2}^0 - \frac{RTJ\delta_{cat}}{n_eFD_{O_2}^{eff}} \quad (25)$$

The inlet hydrogen molar mass flow rate is determined as follows [49]:

$$nH_{2,in} = nH_{2,syngas} + 1(nCO_{syngas}) + 4(nCH_{4,syngas}) \quad (26)$$

The oxygen is dissipated by splitter is calculated through this equation [49]:

$$nO_{2,consumed} = 0.5nH_{2,consumed} = U_a nO_{2,in} \quad (27)$$

$$nH_{2,consumed} = U_f nH_{2,in} \quad (28)$$

$$nH_{2,in}\left(\frac{kmol}{hr}\right) = \frac{1}{2FU_f} \times \frac{3600}{1000} \quad (29)$$

$$nFuel_{in}\left(\frac{kmol}{hr}\right) = \frac{nH_{2,in}}{yH_2 + yCO + 4yCH_4} \quad (30)$$

Where U_a and U_f denote the split fraction of oxygen and fuel utilization coefficient of hydrogen, respectively. Ultimately, power generated is calculated by Equation (31) [52]:

$$P_{DC} = VI \quad (31)$$

Table 3: characteristics of applied solid oxide fuel cell [46]

Parameter	Value	Parameter	Value
Anode thickness (μm)	750	Cathode thickness (μm)	30
Anode pore radius (μm)	0.5	Cathode pore radius (μm)	0.5
Anode particle diameter (μm)	2.5	Cathode particle diameter (μm)	2.5
Anode specific area (1/m)	1.025×10^5	Cathode porosity (dimensionless)	0.48
Anode porosity (dimensionless)	0.35	Cathode tortuosity (dimensionless)	5.4
Anode tortuosity (dimensionless)	3.8	Cathode charge-transfer coefficient (dimensionless)	0.5
Anode charge-transfer coefficient (dimensionless)	0.5	Electrolyte thickness (μm)	25
Interconnect thickness (μm)	1500	Current density A/(cm^2)	0.57
The amount of hydrogen produced (kgmol/h)	6.402	Cell voltage (V)	0.85
Fuel utilization	0.7420	Effective area per cell (m^2)	0.2
Total generated power (kW)	216.4	Cell number	223
O2 usage (kgmol/h)	1.249	Current (A)	254650
Ambient temperature (ºC)	25	Ambient pressure (bar)	1
Power density W/(cm^2)	0.4845		

All the other parameters required are listed in Table 3.

Carbon dioxide power cycle

In this study, a trans-critical carbon dioxide cycle with regeneration and recompression was considered based on the literature [53], and adapted with the proposed integrated structure intended to capture the waste heat from the downstream of the SOFC system and convert it to electricity. According to the literature [53], among various configurations of carbon dioxide power cycles, the trans-critical CO_2 cycle with regeneration and recompression has the highest thermodynamic efficiency [54].

As can be seen in Fig. 2 released heat from the SOFC part and reactor (R300) treat as a low-grade heat source for trans-critical carbon dioxide cycle. High-temperature stream A25 at 1127.2 ˚C released its heat through the HX12 exchanger and heated up stream A59 to 1000 ˚C, which is ready for bringing electricity about 370.5 kW in the T3 turbine. The power generated by the turbine is expressed as [55]:

$$\dot{W}_T = \dot{m}_{CO_2}(h_{59} - h_{60}) \quad (32)$$

Where h_{59} and h_{60}stand for the inlet and outlet enthalpy to the T3 turbine, respectively. While the isentropic efficiency is given by [55]:

$$\eta_T = \frac{h_{59} - h_{60}}{h_{59} - h_{60,s}} \quad (33)$$

Supplied heat, which is derived from the SOFC part, can be defined as follows [56]:

$$\dot{Q}_{in} = \dot{m}_{CO_2}(h_{59}\text{-}h_{58}) = \dot{m}_{25}C_{p,25}(T_{25}\text{-}T_{26}) \quad (34)$$

Expanded carbon dioxide is introduced to HX11, HX10 for missing its heat in two cascades, which can be considered a condenser unit in the conventional model, at 775.8 ˚C and 361 ˚C, respectively. Energy and mass balance of mentioned equipment is stated by [57]:

$$\dot{Q}_{out} = \dot{m}_{60}(h_{60}\text{-}h_{47}) = \dot{m}_{57}(h_{58}\text{-}h_{57}) + \dot{m}_{43}(h_{44}\text{-}h_{43}) \quad (35)$$

$$\dot{m}_{60} = \dot{m}_{57} \quad (36)$$

Stream A47 is divided into two streams for compression stages. Part of the CO_2 stream (A48) with 2058.1 kg/h is passing through two compression stages, while the second one (A46) is carrying 1041.9 kg/h in both 85 ˚C. Due to heating up the flow steam in compression stages, three heat exchangers are applied to the first portion to adapt the carbon dioxide with the inlet pressure of the P3 pump. Power consumed by pump is calculated as follows [58]:

$$\dot{W}_P = \dot{m}_{CO_2}(h_{43} - h_{42}) \quad (37)$$

Organic Rankine cycle

Based on environmental concerns, organic Rankine was applied as a viable and eco-friendly cycle to recycle the heating duty of the heat source with low heat content [59]. The basic concept of the ORC and Rankine cycle is the same, while the ORC uses different working fluids. This working fluid should also meet the operating conditions to generate electricity from the dissipated heat of the SOFC cycle. Considering that, R113 as working fluid release heating duty 129.3 kW to ORC from the upward cycle in an adapted heat exchanger (HX5). Therefore, stream A31, which is preheated by a turbine outlet to 134 ˚C, reaches about doubled temperature means at 260 ˚C until generating electricity by the T1 turbine about 8.977 kW. The second turbine stage is placed back of the first turbine where pressure drop-down at 1500 kPa level, absorbs part of the flow (stream A33) with a flow rate of 2300 kg/h from stream A34 with 229.5 ˚C to generate the 16.55 kW. Table 4 shows the operating properties of numerous streams. Detailed characteristics of the equipment are listed in Table 5.

RESULTS AND DISCUSSION

The lack of research in the field of integrating plasma gasification as high-technological gasification with high efficiency, and eco-friendly cycles were incentive to combine a novel plasma gasification melting with three sub-systems. Syngas released from the MSW plasma gasification process is fed to the SOFC section for generating two other cycles simultaneously. All systems are modeled in Aspen HYSYS/PLUS and MATLAB programming. The main parameters were addressed before are tabulated in Table 6. In this section, the results of the proposed model are compared in SOFC and gasification parts to verify the accuracy of the research. On the other hand, the effect of varying parameters on different components has been investigated comprehensively.

Model validation

Based on five major parameters, validation of the synthesis gases emitted by the gasification process is conducted according to referenced articles, under both experimental model and theoretical data [40, 62]. Results prove an appropriate approval with referenced articles as shown in Fig. 4a.

Fig. 4b demonstrates the effect of current density on cell voltage at different temperatures of the cell. The outcomes show close agreement between investigated model and mentioned article in which the adaption gets closer at higher temperatures [63].

In addition, the specifications of the validated model are listed in Table 7.

Sensitivity analysis

With respect to design parameters, sensitivity analysis is carried out to reflect the system performance under varying required variables.

A well-known curve expressed the cell voltage and power density as a preliminary analysis, renowned by means of a polarization curve. Fig. 5 displays the selected SOFC with detailed operational conditions listed in Table 3, under specific pressure and temperature of 1 bar, 800 K. The cell voltage drops slightly at first, while the power density touches the maximum value of 1191.1 mW/cm^2 at 2.98 A/cm^2 and then falls down. The operation condition of the mentioned system is referenced at 484.5 mW/ cm^2 and 0.85 V of power density and voltage, at a current density of 0.57 A/cm^2.

A valuable analysis is considering the behavior of selected fuel cell under different pressure by the term of altering the operational pressure. In this term, Fig. 6a plotted the power density versus current density by increasing operational pressure. Results show that the effect of increasing pressure on power density is more significant in lower pressures.

To generate stable power electricity, it is worth mentioning that the current density should be in the region of resistance drop being far away from the concentration part. Increasing the current density leads to a large increase in the concentration voltage drop, which in turn will severely reduce the output power and voltage of the cell.

Fig. 6b illustrates the effect of varying operating pressure on cell voltage over current density between 1 bar and 9 bar. It is clear that increasing pressure operation enhances the cell voltage due to intensification of the amount of partial pressure of H_2. However, the growth rate of cell voltage tends to get smaller at upper pressures. Besides, as it is shown, concentration overvoltage plays a major role at lower pressure.

Fig. 7a and Fig. 7b represent the effect of altering operation temperature ranges between 800 °C to 1100 °C in constant pressure of the polarization curve. Fig. 7a shows the effect of temperature on power density at different current densities. It is obvious that a positive

Table 4: The operating characteristics of various streams

Stream	Temperature (ºC)	Pressure (kPa)	Mass flow (kg/h)	Molar Enthalpy (kJ/kgmole)	Molar Entropy (kJ/kgmole.°C)
A1	300.1	129.0	555.4	-113627.4	188.0
A2	557.3	129.0	555.4	-104525.2	201.1
A3	642.5	129.0	0.0	-104525.2	202.1
A4	642.5	129.0	555.4	-104525.2	202.1
A5	770.0	127.0	555.4	-99555.3	207.3
A6	768.5	127.0	755.8	-76704.5	206.8
A7	761.3	127.0	200.4	23889.7	182.7
A9	57.9	134.0	2600.0	955.6	152.4
A10	480.0	129.0	2600.0	13892.7	177.8
A12	269.2	114.5	3155.4	-58805.6	179.3
A13	61.0	114.5	1431.0	-65405.9	163.9
A14	482.1	114.5	1262.1	-51711.9	190.3
A15	139.2	114.5	3155.4	-62964.1	170.5
A16	784.1	124.0	6431.5	23771.1	188.8
A17	891.1	124.0	3831.5	27319.1	191.7
A18	793.2	127.0	6431.5	24072.3	188.9
A19	761.3	127.0	6231.1	22988.3	187.6
A25	1127.2	122.0	3155.4	-28391.9	211.9
A26	780.9	122.0	3155.4	-41215.6	201.4
A28	746.9	119.5	1262.1	-42439.7	200.4
A29	746.9	119.5	462.3	-42439.7	200.4
A30	301.8	119.5	462.3	-57742.3	180.8
A31	134.0	2500.0	2300.0	-703280.3	542.1
A32	260.0	2500.0	2300.0	-665352.9	623.7
A33	229.5	1000.0	2300.0	-667986.5	625.0
A34	229.5	1000.0	1495.0	-667986.5	625.0
A35	171.2	80.0	1495.0	-675455.6	629.3
A36	25.0	100.0	8759.3	-286220.7	53.7
A37	35.0	100.0	8759.3	-285443.6	56.3
A38	28.0	80.0	1495.0	-722815.6	487.6
A39	28.4	1000.0	1495.0	-722685.5	487.7
A40	229.5	1000.0	805.0	-667986.5	625.0
A41	132.3	1000.0	2300.0	-703540.9	541.9
A42	30.8	7682.0	2058.1	-402343.1	112.0
A43	78.0	25110.0	2058.1	-400371.1	113.9
A44	353.0	25100.0	2058.1	-381350.7	155.3
A45	374.8	25100.0	1041.9	-380139.8	157.2
A46	85.0	2280.0	1041.9	-392128.5	152.3
A47	85.0	2280.0	3100.0	-392128.5	152.3
A48	85.0	2280.0	2058.1	-392128.5	152.3
A49	35.0	90.0	2486.3	-285557.1	55.9

Stream	Temperature (ºC)	Pressure (kPa)	Mass flow (kg/h)	Molar Enthalpy (kJ/kgmole)	Molar Entropy (kJ/kgmole.°C)
A50	25.0	100.0	2486.3	-286356.0	53.3
A51	31.9	2270.0	2058.1	-394486.2	145.3
A52	86.7	4055.0	2058.1	-392627.1	146.6
A53	31.9	4045.0	2058.1	-395417.2	138.2
A54	93.1	7692.0	2058.1	-393566.0	139.4
A55	35.0	90.0	9255.9	-285557.1	55.9
A56	25.0	100.0	9255.9	-286356.0	53.3
A57	360.3	25100.0	3100.0	-380943.7	155.9
A58	747.1	25090.0	3100.0	-359506.2	182.3
A59	1100.0	25090.0	3100.0	-339126.8	199.5
A60	775.8	2300.0	3100.0	-358063.3	204.2
A61	361.0	2290.0	3100.0	-379500.8	178.3
A62	25.0	100.0	2942.3	-286356.0	53.3
A63	35.0	90.0	2942.3	-285557.1	55.9
64	746.9	119.5	1431.0	-42439.7	200.4

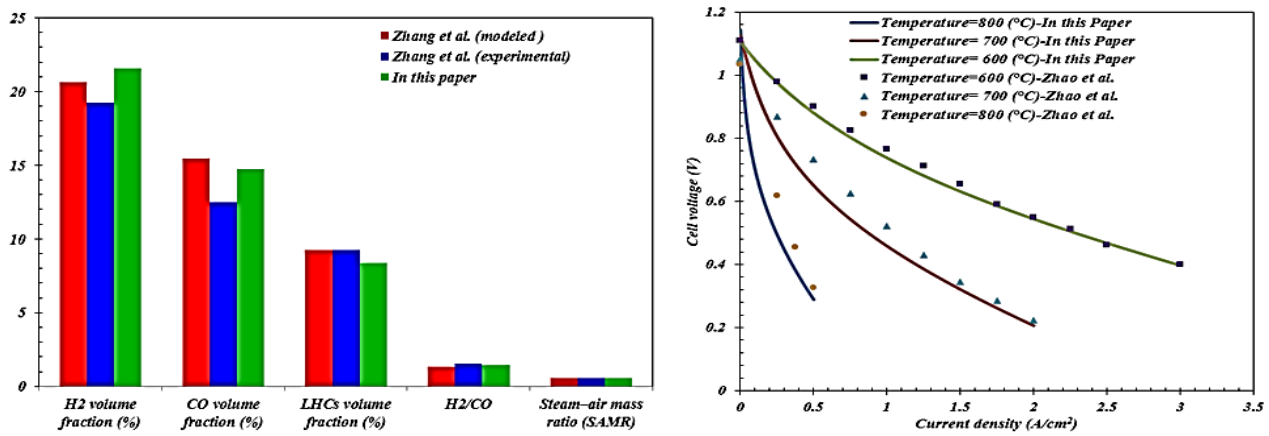

Fig. 4: Validation of a) MSW gasification process with refrenced articles (Zhang, Dor et al. 2012, Zhang, Dor et al. 2012), and b) polarization diagram with mentioned article in different temperature

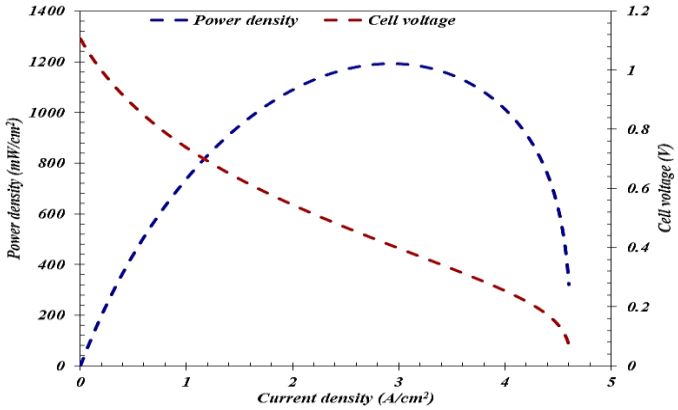

Fig. 5: Variation of voltage and power density of the simulated SOFC

Table 5: Detailed characteristics of the equipment

Pump	Adiabatic Eff.(%)	Power(kW)	ΔP (kPa)	P ratio (-)
P1	85.00	0.8885	1500	2.500
P2	85.00	0.2882	920.0	12.50
P3	85.00	25.62	17428	3.269
Compressor	Adiabatic Eff. (%)	Power(kW)	ΔP (kPa)	P ratio (-)
C1	75.00	11.20	27.70	1.273
C2	75.00	24.09	32.70	1.323
C3	75.00	16.78	3.000	1.024
C4	75.00	18.74	22734	10.61
C5	75.00	78.84	3647	1.902
C6	75.00	24.04	1699	1.721
Turbine	Adiabatic Eff.	Power(kW)	ΔP (kPa)	P ratio (-)
T1	80.00	8.977	1500	0.4000
T2	80.00	16.55	920.0	0.0800
T3	80.00	370.5	22704	0.0951
Heat exchanger	Min. Approach(ºC)	LMTD (ºC)	Duty(kW)	Hot Pinch Temp. (ºC)
HX1	1.660	40.61	69.71	301.7
HX2	10.88	41.12	38.06	780.8
HX3	2.108	30.62	115.3	482.1
HX4	3.060	63.61	323.9	60.96
HX5	5.174	6.990	129.3	139.2
HX6	3.000	35.32	105.1	28.00
HX7	5.800	22.73	114.0	30.80
HX8	6.900	22.28	36.24	31.90
HX9	6.900	21.79	30.63	31.90
HX10	6.988	7.482	247.1	85.00
HX11	1.920	8.041	507.8	361.3
HX12	27.22	30.39	398.8	1127
Reactor	Temperature(ºC)	Pressure(kPa)	Duty(kW)	Type
DECOMP	256.1	101.3	240.2	RYield
COMBUST	479.6	101.3	-240.2	RGibbs
GASIF	756.5	101.3	0	RGibbs
DRYER	256.2	101.3	0	RStoic

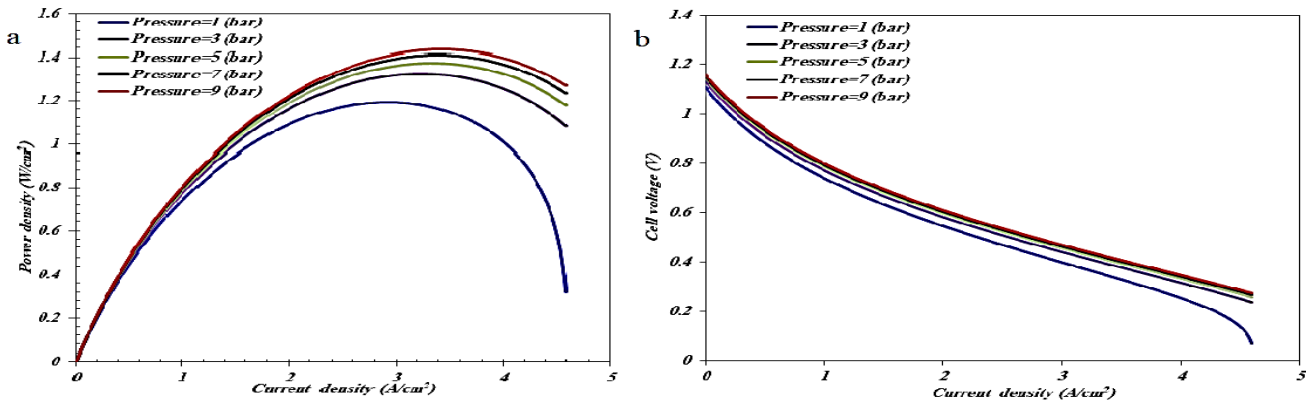

Fig. 6: a) Effect of power density versus current density of the simulated SOFC, b) Influence of cell voltage on current density of the simulated SOFC in different pressures and constant temperature (800 °C)

Table 6: Performance criteria of the diffrent sections in integrated structure

Parameter	Equation	Value
Transcritical carbon dioxide power generation cycle efficiency [58]	$\eta_{CO_2\ \text{power cycle}} = \frac{\dot{W}_{net}}{\dot{Q}_{\text{Inlet to power cycle}}}$	0.5464
SOFC Overall efficiency (LHV) [60]	$\eta_{SOFC} = \frac{\dot{W}_{DC} - \dot{W}_{Compressors} - \dot{W}_{Pumps} + \dot{Q}_{\text{Inlet to power cycles}}}{\dot{m}_{Syngas} \times LHV_{Syngas}}$	0.6122
Power cycles overall thermal efficiency (LHV) [61]	$\eta_{\text{Power cycles}} = \frac{\dot{W}_{Turbines} - \dot{W}_{Compressors} - \dot{W}_{Pumps} + \dot{W}_{DC}}{\dot{m}_{Syngas} \times LHV_{Syngas}}$	0.3987
Gasification process energy efficiency [61]	$\eta = \frac{\dot{m}_{Syngas}.\, LHV_{Syngas}}{\dot{m}_{MSW}.\, LHV_{MSW} + Q_{Steam} + Q_{Plasma}}$	0.5559
Overall thermal efficiency (LHV) [61]	$\eta = \frac{\dot{W}_{Turbines} - \dot{W}_{Compressors} - \dot{W}_{Pumps} + \dot{W}_{DC}}{\dot{m}_{MSW}.\, LHV_{MSW} + Q_{Steam} + Q_{Plasma}}$	0.2153
Plasma energy ratio [40]	$PER = \frac{Q_{Plasma}}{\dot{m}_{MSW}.\, LHV_{MSW}}$	0.1495
Equivalence ratio [40]	$ER = \frac{(\dot{m}_{air}/\dot{m}_{MSW})}{(\dot{m}_{air}/\dot{m}_{MSW})_{stoic}}$	0.061
Steam–air mass ratio [40]	$SAMR = \frac{\dot{m}_{steam}}{\dot{m}_{air}}$	0.556

Table 7: Configuration of validated SOFC model for verification [63]

Parameter	Value	Parameter	Value
Faraday constant (sA/mol)	96485.3	Universal Gas Constant (J/mol.K)	8.314
Pre-exponential factor anode (A/m^2)	6.54×10^{11}	Anode thickness (μm)	1000
Pre-exponential factor cathode (A/m^2)	2.35×10^{11}	Cathode thickness (μm)	20
Anode activation energy (J/mol)	1.4×10^{5}	Interconnect thickness (μm)	20
Cathode activation energy (J/mol)	1.37×10^{5}	Electrolyte thickness (μm)	8
Reference pressure (bar)	1	Anode porosity (dimensionless)	0.48
Pressure (bar)	1	Anode tortuosity (dimensionless)	5.4
Partial pressure of H_2O (bar)	0.03	Average pore radius (μm)	0.5
Partial pressure of H_2 (bar)	1-yH_2O	Average grain size (μm)	1.5
Partial pressure of O_2 (bar)	0.21	Anode ohmic (1/ohm.m)	$(9.5\times10^{7}/T)\times\exp(-1150/T)$
Partial pressure of H_2 (bar)	P×yH_2	Cathode ohmic (1/ohm.m)	$(4.2\times10^{7}/T)\times\exp(-1200/T)$
Partial pressure of H_2O (bar)	P×yH_2O	Electrolyte ohmic (1/ohm.m)	$(3.34\times10^{4})\times\exp(-10300/T)$
Partial pressure of O_2 (bar)	P×yO_2	Interconnect ohmic (1/ohm.m)	(9.3e5/T)×exp(-1100/T)

temperature gradient conducts the power density to reach maximum. Nevertheless, irreversible losses are caused by concentration voltage taking over in a larger amount of current density until it drops sharply. Although the maximum point seems to be the optimal design value, its proximity to the drop region is extremely dangerous for the cell, which should be considered. As can be seen, the effect of temperature gradient on the power density is more noticeable at lower temperatures.

Fig. 7b displays the influence of the operating temperature of the cell on varying cell voltage versus current density. As it is illustrated, increasing in cell temperature reduces voltage drops as a result of facilitating the rate of chemical reactants. This voltage reduction will become more insignificant at higher temperatures. It can be realized that the Open-Circuit Voltage (OCV), which implies the cell voltage in zero current density, decreases slightly at higher temperatures. This result is obtained from the Nernst equation, mentioned (15) to range its value from 1.071 V to 1.017 V by altering the temperature from 800 °C to 1100 °C. Activation voltage drops in lower current densities treat drastically, whereas the Ohmic loss drops depend on temperature linearly.

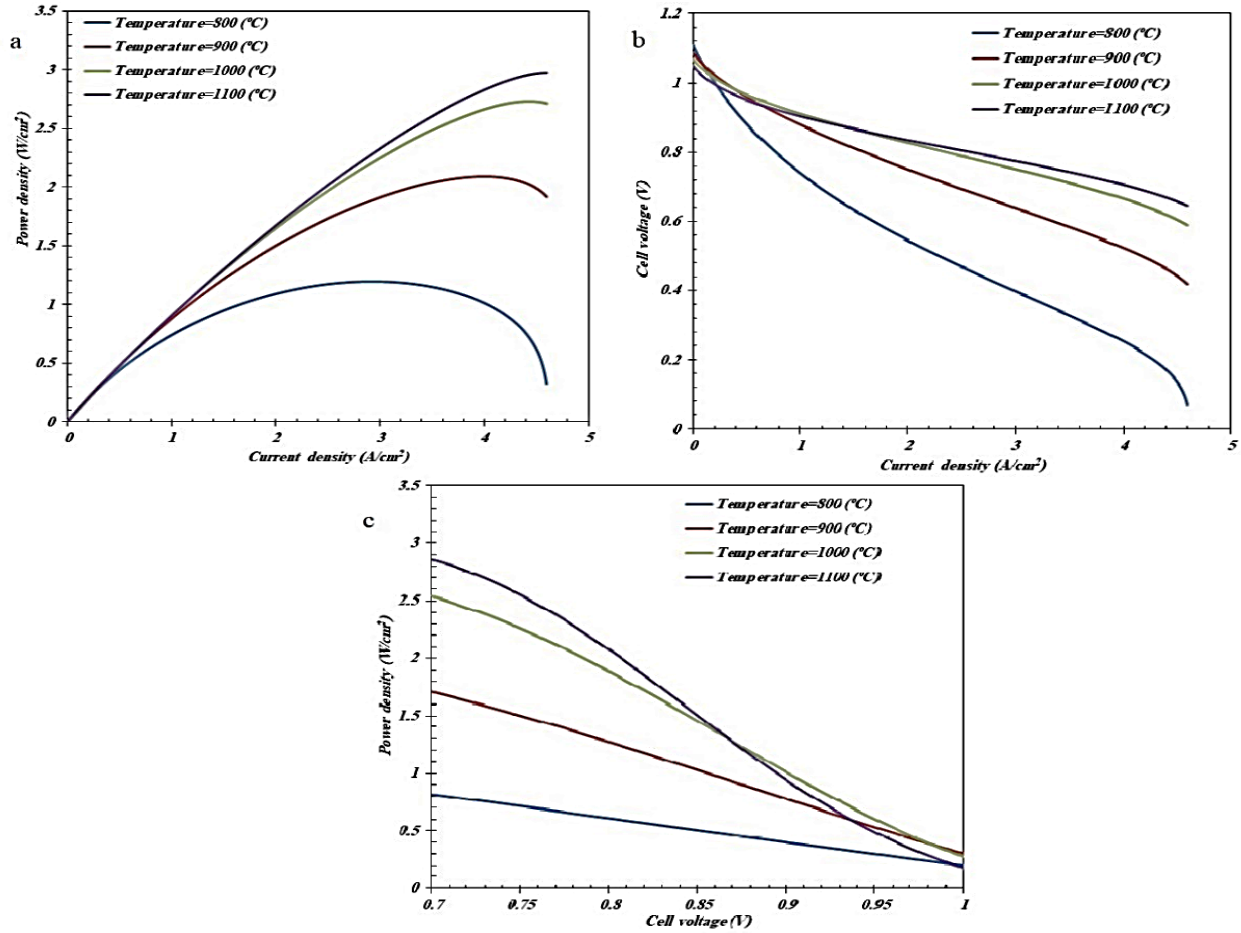

Fig. 7: a) Variations of power density and current density in different temperature and constant pressure, b) Variations of cell voltage and current density in different temperature and constant pressure. c) Variations of power density and cell voltage in different temperature and constant pressure

As reported by Fig. 7a and Fig. 7b the effect of altering the temperature on cell performance was realized more visible than the varying operating pressure. Fig. 7c plotted based on data extracted from Fig. 7a and Fig. 7b. It explains the behavior of power density across cell voltage in different operating temperatures. Large ranges difference in power density (from 0.70 W/cm^2 to 2.83 W/cm^2) in cell voltage of 0.7 V reaches to relatively close amount of power density in 1V. Almost linear behavior of the cell in lower temperatures resulting from Ohimc losses effects.

The effect of air mass flow rate on the mass fraction of syngas produced by PGM is investigated in Fig. 8a, while the syngas compositions have significant weight as the feed of cell on the integrated structure. It resulted that the mass percentages of N_2 and CO_2 as noncombustible gases are directly affected by increasing air flow rates of 47.36% and 75 %, respectively. This appears for the H_2O and CO by decreasing the mass percentages about by 30% and 35%, individually. This can be explained as two major effects of increasing the air flow rate in the reactor. First is enhancing the chemical reactants of the combustion part, which have a positive impact on the produced syngas and its amount of Low Heating Value (LHV). The second is burning the flammable gases due to the facilitated operation of combustion, whereas the amount of N_2, which has a negative impression on exhausted syngas, was increased simultaneously. In addition, increasing the air flow rate causes a moderate reduction in methane production, whereas no sensible effect on hydrogen production. In accordance with increasing air injection, the unchangeable content of H_2 denotes that the amount of hydrogen produced is increasing, which is the result of the second pyrolysis step.

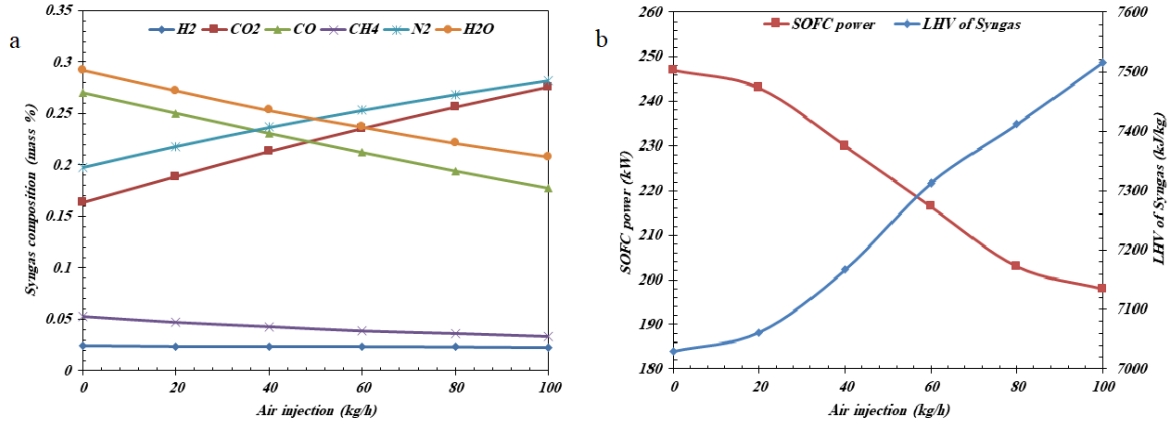

Fig. 8: Effect of air injection on a) syngas compostion produced from gasification of MSW ,b) power produced by SOFC and LHV of syngas exhausted from gasification of MSW

Based on syngas compositions scrutinized in Fig. 8a, LHV of syngas and power generation of SOFC, which is fed from exhausted gas of the gasification process, are represented as shown in Fig. 8b. The amount of LHV starts to increase permanently from 20 kg/h of mass flow injected into the gasification unit. On the other hand, the power generation of SOFC drops from 247 kW to 198 kW by decreasing the content of CO with stable H_2 in syngas compounds. Initially, the fuel cell does not tend to reduce power generation due to the high quality of syngas fed into it.

The mass flow rate of MSW and its influence on two defined efficiencies and syngas temperature was illustrated in Fig. 9a. With increasing the MSW flow rate, the LHV of syngas starts to reduce, which causes the overall thermal efficiency (LHV) and gasification process energy efficiency. Syngas temperature also reduces from 326 ˚C to 250 ˚C by sliding the MSW flow rate from 250 kg/h to 400 kg/h.

Fig. 9b shows the effect of fuel flow rate in beside of net power output generated by three aforementioned cycles and syngas flow rate. The result without any doubt is increasing mass fuel ratio rising syngas flow rate, which ranges between 315 kg/h to 510 kg/h and net power output diminished from 490.6 kW to 330 kW. This reduction can result from the lower quality of syngas as a substitute gaseous fuel for fuel cell and three subsystems driven by its hot utility.

As discussed before, the positive slope of MSW flow rate to air injection and air injection to syngas flow rate causes the rising of the syngas flow rate with MSW mass ratio, which is shown by Fig. 9c. This figure also shows the syngas output temperature is increasing as a result of the heating supply for gasification and pyrolysis by injected air from 245.23 ˚C to 327.16 ˚C.

In addition, increasing the mass flow rate of injected air in the gasifier has become more valuable when it shows its effect on two main efficiencies and net power output provided by the integrated cycle as shown in Fig. 9d. Mitigating the net power output from 432 kW to 375 kW with regard increasing the mass flow rate of injected air in the gasifier is obtained. Results show increasing the gasification process energy efficiency increases from 45.86% to 62.24% due to its equation mentioned in Table 6.

CONCLUSIONS

In this paper, innovative MSW-driven plasma gasification was integrated with solid oxide fuel cell, carbon dioxide, and organic Rankine power cycle. Plasma gasification as a promising technology aimed to convert the disposal of solid waste to high calorific synthesis gas in an eco-friendly manner. This process was addressed in four subsystems; drying, pyrolysis, gasification, and melting, which is investigated by Aspen PLUS. To study the effect of air injection and mass flow rate of MSW on system performance, the model was validated against experimental and theoretical papers, which was confirmed its reasonable accuracy. The MSW with a mass rate of 300 kg/h flows from upward in the opposing direction of high valuable gas with a mass flow rate of 555.4 kg/h at 256.8 °C temperature from downward. Air and steam are injected from

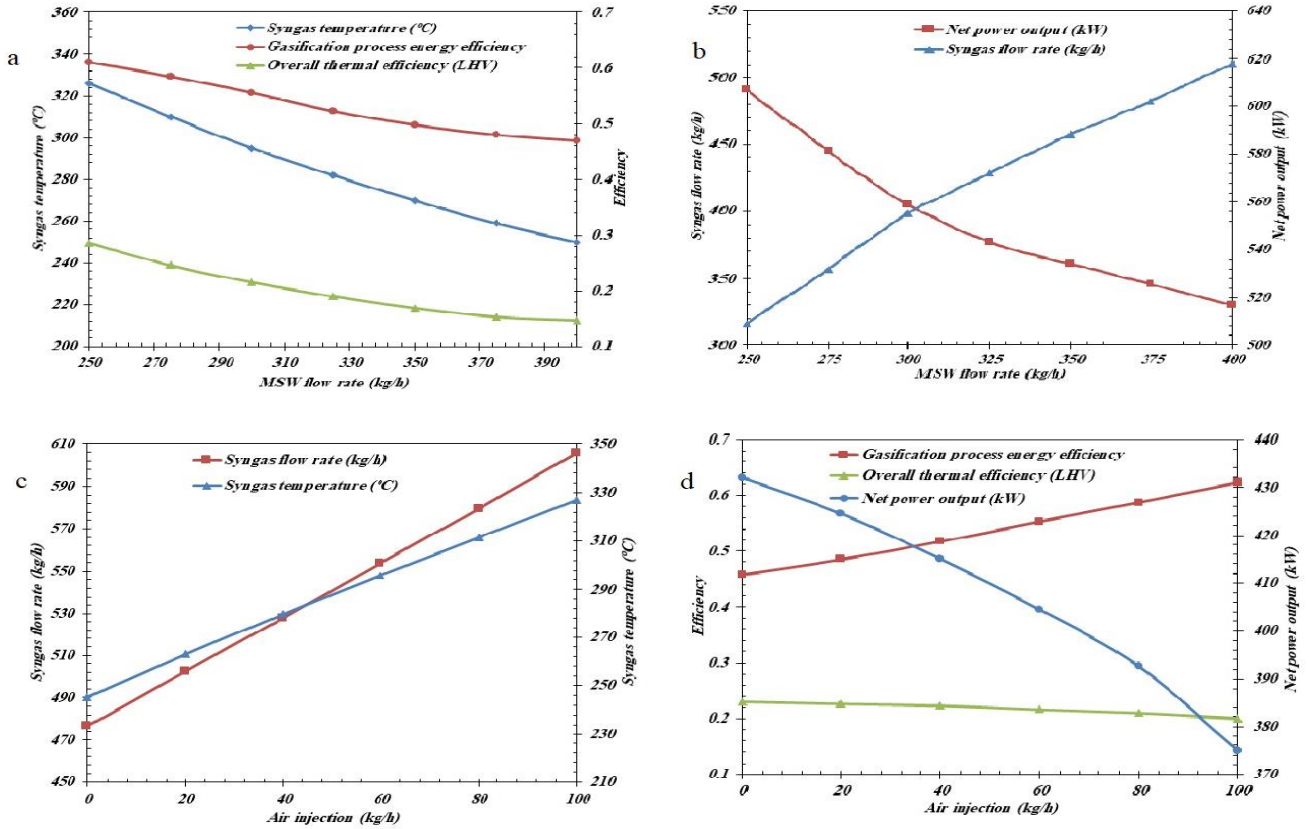

Fig. 9: Effect MSW flow rate on : a) syngas temperature, gasificatoin process and overall thermal efficiency, b) syngas flow rate and net power output generated by developed integrated structure. Effect of injected air flow rate on : c) flow rate and temperature of syngas, d) net power output, overall thermal and gasification process efficiency

downward as agents of gasifier with 60 kg/h and 100 kg/h. To give better insight into system performance, PER, ER, SAMR are introduced as three dimensionless numbers are calculated at 0.1495, 0.061, and 0.556, respectively. The SOFC system is fed by synthesis gas produced from the gasification process to bring 162.3 kW power with 61.22% efficiency. The polarization curve of SOFC process was validated with the referenced article to verify the model. Dissipated heat from SOFC cycle introduced to organic Rankine and carbon dioxide plant through heat exchangers to generate 24.35 kW and 217.8 kW power in 18.83 % and 54.64%, respectively. Increasing injected air shifting from 0 kg/h to 100 kg/h causes the increase in the amount of N_2, CO_2, while the opposite occurred for H_2O, CO, and CH_4. On the other hand, the syngas temperature and syngas flow rate are increased from 245.23 °C to 327.16 °C and 476.62 kg/h to 605.69 kg/h, correspondingly. Despite of increasing the amount of LHV of syngas, the power generated by the SOFC plant is reduced from 247 kW to 198 kW. The mass flow rate of MSW was also scrutinized by increasing its value between ranges 250 kg/h to 400 kg/h. It was shown that all syngas temperature, gasification process energy efficiency, overall thermal efficiency, and net power output were decreased while the syngas was improved. The exergy and economic studies of the hybrid structure can be assessed in future investigations. Exergeoeconomic and advanced exergy examinations of the combined system can also be considered as a future analysis approach.

Conflict of interest statement

The authors declare that they have no known competing financial interests or personal relationships that could have appeared to influence the work reported in this paper.

Nomenclature

CHP	Combined Heat and Power
Ci	Compressor

ER	Equivalence ratio
HHV	High heating value
HXi	Heat exchanger
LHV	Low heating value
MSW	Municipal solid waste
ORC	Organic Rankine cycle
PER	Plasma energy ratio
PGM	Plasma Gasification Melting
Pi	Pump
SAMR	Steam air mass ratio
SG	Synthesis Gas
SMR	Synthesis gas production reactor
SOFC	Solid oxide fuel cell
Ti	Turbine
WGS	Water – Gas shifting
WtE	Waste to Energy
CO	Carbon monoxide
CO_2	Carbon dioxide
CH_4	Methane
H_2	Hydrogen
H_2O	Water
N_2	Nitrogen
O_2	Oxygen
A	Area(m^2)
C_p	Heat capacity (kJ /kg. K)
D_i^{eff}	Effective diffusion coefficient of species i ($cm^2.s^{-1}$)
F	Faraday constant, 96,485 (C/mol)
h_i	Specificenthalpyatpoint i(kJ/kg)
h_{ev}	Evaporation enthalpy of water (kJ kg^{-1})
I	Current(A)
J	Current density (A /cm^2)
J_0	Exchange current density (A/cm^2)
$\dot{m}$	Mass flow rate (kg /s)
n_e	Moles number of electron transferred
P_i	Partial pressure of species i (bar)
P_i^*	Reaction site partial pressure of species i (bar)
P_i^0	Bulk partial pressure of species i (bar)
P_{DC}	Fuel cell power output (kW)
$\dot{Q}$	Heating(kW)
R	Universal gas constant (J/mol. K)
T	Temperature (^oK)
U_f	Fuel utilization coefficient
V	Actual voltage (V)
$\dot{W}$	Power(kJ/kg)
σ	Ionic or electronic conductivity($\Omega^{-1}cm^{-1}$)
δ	Thickness (cm)
act	Activation
an	Anode
cat	Cathode
conc	Concentration
CO_2	Carbon dioxide
dry	dry
H_2O	Moisture
i	Species i
in	Inlet
MSW	Municipal solid waste
out	Outlet
ohm	Ohmic
Plasma	Plasma
steam	Steam

Received : Oct. 11, 2022 ; Accepted : Jan. 16, 2023

REFERENCES

[1] Khan A.H., et al., Municipal Solid Waste Generation and the Current State of Waste-to-Energy Potential: State of Art Review, *Energy Conversion and Management*, **267**: 115905 (2022).

[2] Omidi Kashani B., Khoshbakhti Saray R., Kheiri R., Modeling and Thermodynamic Analysis of Municipal Solid Waste Dryer: A parametric Study, *Iranian Journal of Chemistry and Chemical Engineering (IJCCE)*, **41(8):** 2848-2872 (2022).

[3] Mboowa D., et al., Qualitative Determination of Energy Potential and Methane Generation from Municipal Solid Waste (MSW) in Dhanbad (India), *Energy*, **123**: 386-391 (2017).

[4] Shoeibi H., et al., Transient Simulation and Exergy Analysis of Heat-Pump Systems Integrated with Solar Compound Parabolic Collector, *Iranian Journal of Chemistry and Chemical Engineering (IJCCE)*, **41(6)**: 2121-2134 (2022).

[5] Munir M.T., et al., Plasma Gasification of Municipal Solid Waste for Waste-to-Value Processing, *Renewable and Sustainable Energy Reviews*, **116**: (2019).

[6] Dastjerdi B., et al., An evaluation of the Potential of Waste to Energy Technologies for Residual Solid Waste in New South Wales, Australia, *Renewable and Sustainable Energy Reviews*, **115**: (2019).

[7] Izquierdo-Horna L., Kahhat R., Vázquez-Rowe I., Reviewing the Influence of Sociocultural, Environmental and Economic Variables to Forecast Municipal Solid Waste (MSW) Generation, *Sustainable Production and Consumption*, **33**: 809-819 (2022).

[8] Hosseini S.S., et al., Introducing, Evaluation and Exergetic Performance Assessment of a Novel Hybrid System Composed of MCFC, Methanol Synthesis Process, and a Combined Power Cycle, *Energy Conversion and Management*, **197** (2019).

[9] Petroleum B., "BP Energy Outlook, 2020 edition, London (2020).

[10] Dong J., et al., Key Factors Influencing the Environmental Performance of Pyrolysis, Gasification and Incineration Waste-to-Energy Technologies, Energy Conversion and Management, **196**: 497-512 (2019).

[11] Amodeo C., et al., Temperature Phased Anaerobic Digestion (TPAD) of Organic Fraction of Municipal Solid Waste (OFMSW) and Digested Sludge (DS): Effect of Different Hydrolysis Conditions, *Waste Management*, **126**: 21-29 (2021).

[12] Mahmood R.T., et al., Bioremediation of Textile Industrial Effluents by Fomitopsis Pinicola IEBL-4 for Environmental Sustainability, *Human and Ecological Risk Assessment: An International Journal*, 1-18 (2022).

[13] Shumal M., et al., Comprehensive Analysis of Municipal Solid Waste Rejected Fractions as a Source of Refused Derived Fuel in Developing Countries (Case Study of Isfahan- Iran): Environmental Impact and Sustainable Development, *Renewable Energy*, **146**: 404-413 (2020).

[14] Wang N., et al., Upgrading Gas and Oil Products of the Municipal Solid Waste Pyrolysis Process by Exploiting In-Situ Interactions between the Volatile Compounds and the Char, *Waste Management*, **102**: 380-390 (2020).

[15] Tavares R., Ramos A., Rouboa A., A theoretical Study on Municipal Solid Waste Plasma Gasification, *Waste Management*, **90**: 37-45 (2019).

[16] Gheewala S., et al., Sensitivity Analysis of Coal and Bagasse Co-Firing in an Integrated Gasification Combined Cycle Power Plant, *Iranian Journal of Chemistry and Chemical Engineering (IJCCE)*, **41(12):** 4269-4281(2022).

[17] Mukherjee C., et al., A review on Municipal Solid Waste-to-Energy Trends in the USA, *Renewable and Sustainable Energy Reviews*, **119** (2020).

[18] Consonni S., Lombardi L., Viganò F., Municipal Solid Waste to Energy Technology, *In Encyclopedia of Sustainable Technologies*, 389-401 (2017).

[19] Janajreh I., Raza S.S., Valmundsson A.S., Plasma Gasification Process: Modeling, simulation and Comparison With Conventional Air Gasification, *Energy Conversion and Management*, **65**: 801-809 (2013).

[20] Rajasekhar M., et al., Energy Generation from Municipal Solid Waste by Innovative Technologies – Plasma Gasification, *Procedia Materials Science*, **10**: 513-518 (2015).

[21] Favas J., Monteiro E., Rouboa A., Hydrogen Production Using Plasma Gasification with Steam Injection, *International Journal of Hydrogen Energy*, **42(16)**: 10997-11005 (2017).

[22] Sauve G., et al., integrated Early-Stage Environmental and Economic Assessment of Emerging Technologies and its Applicability to the Case of Plasma Gasification, *Journal of Cleaner Production*, 134684 (2022).

[23] Barhoumi E.M., et al., Optimal Sizing of Photovoltaic Systems Based Green Hydrogen Refueling Stations Case Study Oman, *International Journal of Hydrogen Energy*, **47(75)**: 31964-31973 (2022).

[24] Mehrpooya M., Ghorbani B., Abedi H., Biodiesel Production Integrated with Glycerol Steam Reforming Process, Solid Oxide Fuel Cell (SOFC) Power Plant, *Energy Conversion and Management*, **206**: (2020).

[25] Pongratz, G., et al., Analysis of H2S-Related Short-Term Degradation and Regeneration of Anode- and Electrolyte Supported Solid Oxide Fuel Cells Fueled with Biomass Steam Gasifier Product Gas, *Energy*, **218** (2021).

[26] Leal E.M., Bortolaia L.A., Leal Junior A.M., Technical Analysis of a Hybrid Solid Oxide Fuel Cell/Gas Turbine Cycle, *Energy Conversion and Management*, **202** (2019).

[27] Chitgar N., et al., Investigation of a Novel Multigeneration System Driven by a SOFC for Electricity and Fresh Water Production, *Energy Conversion and Management*, **196**: 296-310 (2019).

[28] Li, R., et al., Cost-Optimal Operation Strategy for Integrating Large Scale of Renewable Energy in China's Power System: From a Multi-Regional Perspective, *Applied Energy*, **325**: 119780 (2022).

[29] Yang Y., et al., A Techno-Economic Analysis of Energy Recovery from Organic Fraction of Municipal Solid Waste (MSW) by an Integrated Intermediate Pyrolysis and Combined Heat and Power (CHP) Plant, *Energy Conversion and Management*, **174**: 406-416 (2018).

[30] Salman CA S.S., Naqvi M., Thorin E., Yan J., Synergistic Combination of Pyrolysis, Anaerobic Digestion, and CHP Plants, *Energy Procedia*, **158**: 1323-1329 (2019).

[31] Galeno G., Minutillo M., Perna A., From Waste to Electricity through Integrated Plasma Gasification/Fuel Cell (IPGFC) System, *International Journal of Hydrogen Energy*, **36(2)**: 1692-1701 (2011).

[32] Sakhraji M., et al., Plasma Gasification Process Using Computational Fluid Dynamics Modeling, *Energy Reports*, **8**: 1541-1549 (2022).

[33] Chen H., et al., Performance Assessment of a Novel Medical-Waste-to-Energy Design Based on Plasma Gasification and Integrated with a Municipal Solid Waste Incineration Plant, *Energy*, **245**: 123156 (2022).

[34] Lee J., et al., Hybrid Renewable Energy Systems Involving Thermochemical Conversion Process for Waste-to-Energy Strategy, *Chemical Engineering Journal*, **452**: 139218 (2023).

[35] Indrawan N., et al., Modeling Low Temperature Plasma Gasification of Municipal Solid Waste, *Environmental Technology & Innovation*, **15**: (2019).

[36] Ismail T.M., et al., An Eulerian Model for Forest Residues Gasification in a Plasma Gasifier, *Energy*, **182**: 1069-1083 (2019).

[37] Kuo P.C., et al., Plasma Gasification Performances of Various Raw and Torrefied Biomass Materials Using Different Gasifying Agents, *Bioresour Technol*, **314**: 123740 (2020).

[38] Tamošiūnas A., et al., Thermal Arc Plasma Gasification of Waste Glycerol to Syngas, *Applied Energy*, **251** (2019).

[39] Pei S.-L., et al., Addressing Environmental Sustainability of Plasma Vitrification Technology for Stabilization of Municipal Solid Waste Incineration Fly Ash, *Journal of Hazardous Materials*, **398** (2020).

[40] Zhang Q., et al., Performance Analysis of Municipal Solid Waste Gasification with Steam in a Plasma Gasification Melting Reactor, *Applied Energy*, **98**: 219-229 (2012).

[41] Zhang Q., et al., A Thermodynamic Analysis of Solid Waste Gasification in the Plasma Gasification Melting Process, *Applied Energy*, **112**: 405-413 (2013).

[42] Tlili I., et al., Numerical and Experimental Analysis of Temperature Distribution and Melt Flow in Fiber Laser Welding of Inconel 625, *The International Journal of Advanced Manufacturing Technology*, **121(1)**: 765-784 (2022).

[43] Bejan A., Tsatsaronis G., Moran M.J., "Thermal Design and Optimization". John Wiley & Sons Inc. (1996).

[44] Preininger M., et al., Performance of a Ten-Layer Reversible Solid Oxide Cell Stack (rSOC) Under Transient Operation for Autonomous Application, *Applied Energy*, **254** (2019).

[45] Hou K., Hughes R., The Kinetics of Methane Steam Reforming Over a Ni/a-Al2O Catalyst, *Chemical Engineering Journal*, **82**: 311-328 (2011).

[46] Mehrpooya M., Conceptual Design and Energy Analysis of Novel Integrated Liquefied Natural Gas and Fuel Cell Electrochemical Power Plant Processes, *Energy*, **111**: 468-483 (2016).

[47] Hemmatabady H., Mehrpooya M., Mousavi S.A., Development of a Novel Hybrid SOFC/GT System and Transcritical CO2 Cycle for CCHP Purpose in the District Scale, *Journal of Thermal Analysis and Calorimetry* (2020).

[48] Aghaie M., Mehrpooya M., Pourfayaz F., Introducing an Integrated Chemical Looping Hydrogen Production, Inherent Carbon Capture and Solid Oxide Fuel Cell Biomass Fueled Power Plant Process Configuration, *Energy Conversion and Management*, **124**: 141-154 (2016).

[49] Ebrahimi A., et al., Biomass Gasification Process Integration with Stirling Engine, Solid Oxide Fuel cell, and Multi-Effect Distillation, *Journal of Thermal Analysis and Calorimetry* (2020).

[50] Roushenas R., et al., Thermo-Environmental Analysis of a Novel Cogeneration System Based on Solid Oxide Fuel Cell (SOFC) and Compressed Air Energy Storage (CAES) Coupled with Turbocharger, *Applied Thermal Engineering*, **181** (2020).

[51] Reyhani H.A., et al., Thermodynamic and Economic Optimization of SOFC-GT and its Cogeneration Opportunities Using Generated Syngas from Heavy Fuel Oil Gasification, *Energy*, **107**: 141-164 (2016).

[52] Roushenas R., Zarei E., Torabi M., A Novel Trigeneration System Based on Solid Oxide Fuel Cell-Gas Turbine Integrated with Compressed Air and Thermal Energy Storage Concepts: Energy, Exergy, and Life Cycle Approaches, *Sustainable Cities and Society*, **66**: 102667 (2021).

[53] Song Y., et al., Thermodynamic Analysis of a Transcritical CO_2 Power Cycle Driven by Solar Energy with Liquified Natural Gas as its Heat Sink, *Applied Energy*, **92**: 194-203 (2012).

[54] Kazemi H., Shahhosseini S., Amiri M., Optimization of CO_2 Capture Process Using Dry Sodium-Based Sorbents, *Iranian Journal of Chemistry and Chemical Engineering (IJCCE)*, **40(4)**: 1179-1194 (2021).

[55] Razmi A.R., et al., Design, Thermodynamic, and Wind Assessments of a Compressed Air Energy Storage (CAES) Integrated with Two Adjacent Wind Farms: A Case Study at Abhar and Kahak Sites, Iran, *Energy*, **221** (2021).

[56] Ghorbani B., Mehrpooya M., Ardehali A., Energy and Exergy Analysis of Wind Farm Integrated with Compressed Air Energy Storage Using Multi-Stage Phase Change Material, *Journal of Cleaner Production*, **259** (2020).

[57] Farrokhi M., et al., Simulation and Techno-Economic Analysis of the Integration of a Combined Heat and Power System in a Flare Gas Recovery Unit – Case Study: Tabriz Oil Refining Company (Northwest Iran), *Iranian Journal of Chemistry and Chemical Engineering (IJCCE)*, **42(7):** 2318-2331 (2022).

[58] Ahmadi M.H., et al., Thermo-economic Analysis and Multi-Objective Optimization of a Transcritical CO_2 Power Cycle Driven by Solar Energy and LNG Cold Recovery, *Thermal Science and Engineering Progress*, **4**: 185-196 (2017).

[59] Nayak M.K., et al., Entropy Optimized Assisting and Opposing Non-Linear Radiative Flow of Hybrid Nanofluid, *Waves in Random and Complex Media*, 1-22 (2022).

[60] Mehrpooya M., Sharifzadeh M.M.M., Mousavi S.A., Evaluation of an Optimal Integrated Design Multi-Fuel Multi-Product Electrical Power Plant by Energy and Exergy Analyses, *Energy*, **169**: 61-78 (2019).

[61] Mehrpooya M., Esfilar R., Moosavian S.M.A., Introducing a Novel Air Separation Process Based on Cold Energy Recovery of LNG Integrated with Coal Gasification, Transcritical Carbon Dioxide Power Cycle and Cryogenic CO_2 Capture, *Journal of Cleaner Production*, **142**: 1749-1764 (2017).

[62] Zhang Q., et al., Gasification of Municipal Solid Waste in the Plasma Gasification Melting Process, *Applied Energy*, **90(1)**: 106-112 (2012).

[63] Zhao F., Virkar A., Dependence of Polarization in Anode-Supported Solid Oxide Fuel Cells on Various Cell Parameters, *Journal of Power Sources*, **141(1)**: 79-95 (2005).